Journal of The Electrochemical Society, **157** (5) A589-A599 (2010)
0013-4651/2010/157(5)/A589/11/$28.00 © The Electrochemical Society

A Mathematical Model for the Soluble Lead-Acid Flow Battery

A. A. Shah,[z] X. Li,[*] R. G. A. Wills, and F. C. Walsh[*]

Electrochemical Engineering Laboratory, Energy Technology Research Group, School of Engineering Sciences, University of Southampton, Highfield, Southampton SO17 1BJ, United Kingdom

The soluble lead-acid battery is a redox flow cell that uses a single reservoir to store the electrolyte and does not require a microporous separator or membrane, allowing a simpler design and a substantial reduction in cost. In this paper, a transient model for a reversible, lead-acid flow battery incorporating mass and charge transport and surface electrode reactions is developed. The charge–discharge behavior is complicated by the formation and subsequent oxidation of a complex oxide layer on the positive electrode surface, which is accounted for in the model. The full charge/discharge behavior over two cycles is simulated for many cases. Experiments measuring the cell voltage during repeated charge–discharge cycles are described, and the simulation results are compared to the laboratory data, demonstrating good agreement. The model is then employed to investigate the effects of variations in the current density on the performance of the battery.
 [DOI: 10.1149/1.3328520]

Manuscript submitted November 30, 2009; revised manuscript received January 25, 2010. Published April 7, 2010.

The pressing demand for clean and efficient energy conversion, storage, and delivery, particularly the demand for renewable energy, has generated considerable interest in bulk energy storage technologies. Promising candidates for meeting the future energy-storage needs, including microgeneration, include redox flow batteries (RFBs) and flow batteries. In conventional batteries, such as the static lead-acid and lithium-ion cells, energy is stored entirely in the electrode structure. Redox flow batteries store energy either in a liquid electrolyte solution containing different redox couples, as in the all-vanadium battery, or in both an electrolyte and on the electrode surfaces in the form of deposits, as in the zinc–cerium system. The bulk of the electrolyte is stored in (typically two) reservoirs external to the cell.[1] The energy capacity of the system is determined by the volume of electrolytes in the tanks, the reactant concentrations, and the active area of the electrodes, while the system power is limited mainly by the size of the stacks and the active electrode surface area. Flow batteries can use a porous electrode (flow-through design), or the electrolyte can flow past an activated electrode (flow-by design).

The applications of RFBs are not limited to the exploitation of renewable energy resources from the environment on large scales. RFBs can potentially be used for load leveling and peak shaving, uninterruptible power supply, and emergency backup.[2] Demand for electricity is variable, requiring that some power generation installations are operated only during periods of high demand, a highly expensive and inefficient solution. An integrated energy-delivery system that includes an energy storage capability would improve reliability and enhance the quality of the electricity supply. For the supplier, it affords greater flexibility and savings in costs. Surplus installations could be decommissioned with the remaining installations operated at an almost constant load; storage cells would be charged during times of low demand and discharged into the grid during times of peak demand. Established storage technologies, such as static lead-acid and nickel–cadmium cells, have been considered for load leveling but are generally considered to be limited by performance, lifetime, and cost on a large scale. As a result, advanced systems such as RFBs receive a great deal of attention.

The reversible electrode processes in a flow battery involve soluble, solution-based redox species. Electrode processes take place at the surfaces of inert or catalyzed electrodes. The reactants flowing across these electrodes enter from external reservoirs, and the positively charged and negatively charged electrolytes are usually prevented from mixing in the electrochemical cell by an ion-selective membrane or a microporous separator. Typical examples are the all-vanadium, sodium/sulfur, zinc/bromine, and polysulfide/bromine systems.[1,3] An alternative design, based on the electrode reactions of Pb(II) in methanesulfonic acid, has been introduced in a series of papers by Hazza et al., Pletcher et al., Li et al., and Wills et al.[4-9] (referred to here as the "soluble lead-acid battery"). The electrode reactions differ from those in the traditional static lead-acid battery because Pb(II) is highly soluble in the acid. In the static lead-acid battery, Pb(II) is supplied from a paste containing lead sulfate that is coated onto the electrode surfaces.[10] The complexities associated with solid-to-solid conversion are avoided in the soluble lead-acid battery. As a flow battery, the soluble lead acid battery is also unique in that no microporous separator (typically a cation-exchange membrane such as Nafion) is required and a single reservoir is used for the electrolyte, allowing for a simpler design and a substantial reduction in cost.

The current hurdles to full-scale commercialization of flow battery technology are scale-up and optimization, improvement in electrolyte stability, development of electrode materials resistant to oxidation, and mitigation of membrane fouling. At present, flow batteries do not satisfy all the performance requirements and the cost targets demanded by major energy providers, although scale-up is much less an issue than with the traditional batteries. A purely laboratory-based approach to the challenges involved is impracticable due to the financial costs and long time scales required for extensive testing of components, materials, flow geometries, scales, compositions, and additives over a range of operating conditions. Modeling and simulation are important tools to reduce the burden. Although conventional batteries such as the static lead-acid, nickel-metal hydride, and lithium-ion cells,[11-20] as well as fuel cells,[21-23] have been the subject of numerous modeling studies, simulation of flow battery performance is not yet a well-developed area. Notable exceptions include the models developed by Shah et al.[24] and by Li and Hikihara[25] for the all-vanadium system and by Scamman et al.[3] for the bromide–polysulphide battery. There are no models, as far as the authors are aware, of the soluble lead-acid flow battery, even in the simplest cases. In this paper, a transient, two-dimensional model based on conservation principles (mass, momentum, and charge), incorporating the fundamental modes of transport for the charged species and water, is developed. This transport model is combined with a kinetic model that incorporates key side reactions. The resulting numerical code is able to simulate the entire charge–discharge behavior over several cycles.

The next section contains details of experimental flow cell design and operation, preparation of the electrolyte, and data acquisition. Details of the development of the mathematical model, including the underlying assumptions, are provided in the Model Development section. The numerical approach is outlined in detail in the Numerical Details section, where error estimates and convergence are assessed. Simulation results and comparisons to the experimental data are presented in the Results and Discussion section. The effects of the applied current density on the charge–discharge behavior and the efficiency of the cell are investigated. In a forthcoming paper, a wide

* Electrochemical Society Active Member.
[z] E-mail: A.Shah@soton.ac.uk

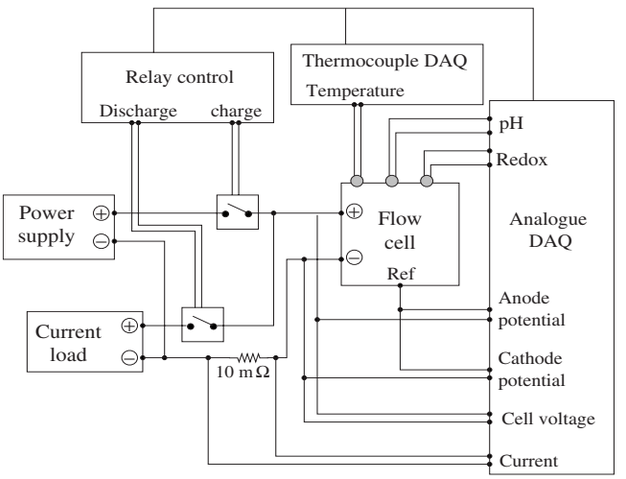

Figure 1. Schematic of the experimental soluble lead-acid battery system.

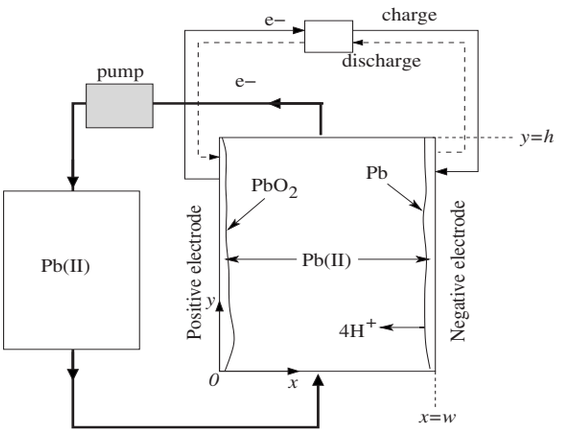

Figure 2. The soluble lead-acid battery and the flow system. The reservoir contains the bulk of the electrolyte, which is pumped through the cell in which reactions occur at the electrode surfaces.

ranging parametric study with further validation will be detailed, including the effects of the temperature, mean linear flow velocity, electrolyte composition, electrode dimensions, and interelectrode gap. The results of the present study are summarized in the Conclusions and Future Development section.

Experimental

The flow cell and flow circuit have been described in detail elsewhere.[26] For the data reported here, carbon polyvinyl ester composite (Entegris) and nickel plate (Goodman Alloys Ltd.) were used for the positive and negative electrodes, respectively. Copper plates ($10 \times 10 \times 0.3$ cm) were used as current collectors. The electrodes were secured to the current collectors using a polypropylene frame (TM Plastics Ltd.) and then masked using insulating tape to protect the copper from corrosion, yielding an exposed electrode area of 10×10 cm for both the positive and negative electrodes. The interelectrode gap of 1.2 cm was established using the polypropylene frame and elastomeric ethylene propylene diene terpolymer gaskets (Klinger), which were placed between frames to seal the cell. The electrolyte comprised lead methane sulfonate, methanesulfonic acid, and hexadecyltrimethylammonium hydroxide: 0.5 M $Pb(CH_3SO_3)_2$ + 0.5 M CH_3SO_3H + 5 mM $C_{16}H_{33}(CH_3)_3N(OH)$. The total volume of the electrolyte was 1500 cm^3, and it was stored in a 2 L cylindrical reservoir and circulated through the system via a pump (Totton Pumps, type T113095) with a mean linear flow velocity of 2.3–6.9 cm s^{-1} past the electrode surfaces. The charge/discharge cycling experiment was carried out using an in-house-developed, computer-controlled charge–discharge and automated logging system. Constant currents were applied and drawn using a dc power supply and load (Thurlby Thandar Instruments, U.K.). The cell voltage was measured directly using a National Instruments data acquisition system. A schematic is shown in Fig. 1.

With the cell configuration described above and with a current density of 10 mA cm^{-2}, the cell power was between 1.5 and 2.5 W. Using an electrolyte volume of 1500 cm^3 and an initial Pb^{2+} concentration in the electrolyte of 0.5 mol dm^{-3}, the cell capacity (assuming a utilization of approximately two-thirds of the theoretical) is approximately 13 Ah. At a discharge voltage of 1.5 V, the energy density of the electrolyte reservoir is approximately 20 Wh dm^{-3}.

Model Development

Assumptions.— The model developed is based on the two-dimensional slice depicted in Fig. 2. The model domain includes the electrodes and the electrolyte, both inside the cell and in the reservoirs. The two-dimensional approximation leads to a considerable saving in computational time without a major loss in accuracy if the electrolyte flow rate is reasonably high, as in normal operation. Extension of the model to three dimensions is straightforward.

It is assumed that the dissociated electrolyte solution [Pb(II) in methanesulfonic acid] is composed of H_2O, H^+, Pb(II), and negatively charged counterions HSO_4^-. Mass balances are derived for each of these components.

Transport of the charged species occurs by diffusion, migration, and convection. All three transport modes are included, although the migration terms are small due to the presence of a high concentration of methanesulfonic acid CH_3SO_3H as an indifferent electrolyte. The dilute-solution approximation is employed, assuming water to be a dominant component. As a consequence, the electrolyte is treated as incompressible. Models of the static lead-acid,[11] nickel-metal hydride,[12,13] and lithium-based[14-16] batteries are typically based on a binary-electrolyte approximation, which is not applicable to the present problem. In the binary electrolyte, concentrated solution theory[27] is straightforward but becomes cumbersome when several species are involved. It is further assumed, as a first approximation, that the thicknesses of the deposited Pb and PbO_2 layers are small compared to the interelectrode gap and are, therefore, neglected. Over long time scales, involving several tens of charge–discharge cycles, the deposited layers can have a major impact on the electrode reactions and on the flow of the electrolyte.[28] Over the time scales considered in this paper (the first two charge–discharge cycles), however, the deposition layers are not critical. The system is assumed to be isothermal. In a forthcoming paper, the effects of temperature variations will be investigated, along with a wider ranging parametric study.

Reaction mechanisms.— The following simplified set of half-reactions is adopted[4]

$$\text{at the negative electrode: } Pb(II) + 2e^- \rightleftharpoons Pb \qquad [1]$$

$$\text{at the positive electrode: } Pb(II) + 2H_2O - 2e^- \rightleftharpoons PbO_2 + 4H^+ \qquad [2]$$

In addition to these reactions, side reactions such as oxygen and hydrogen evolution are known to occur,[4,5] and these reactions consume a portion of the applied current. One of the characteristic features of the soluble lead-acid battery is the "two-step" charge curve seen under a broad range of conditions. On a virgin electrode, the cell voltage during charge is influenced primarily by the redox Reactions 1 and 2 but during the second cycle, charging commences at a significantly lower potential, eventually increasing to the cell potential attained during the first charge phase.[4-9] This phenomenon is understood to be associated with the positive electrode, although

the origins of this behavior are not entirely clear. Pletcher and Wills examined scanning electron micrograph images of a vitreous carbon rotating disk electrode and found that patches of a solid remain on the electrode after discharge.[6] Further X-ray diffraction analysis has shown that the remaining solid is a mixture of α-PbO_2 and β-PbO_2, while the presence of PbO cannot be ruled out[26] because the diffraction peaks coincide with β-PbO_2. The precise nature of the deposit is, however, still not clear. As noted by Pletcher and Wills, this complex oxide deposit could arise during the dissolution of the PbO_2 if the concentration of Pb^{2+} in the boundary layer close to the electrode is high enough to exceed the solubility product of a Pb(II) species or if the proton concentration in the boundary layer approaches zero.[6] The authors further suggested that the deposit is reoxidized to PbO_2 more readily than Pb^{2+} in solution, which leads to the two-step charge process described above. Xi et al.[26] reached the same conclusion using cyclic voltammetry and XRD analysis.

Due to its significant influence on the charge–discharge behavior (and the fact that it leads to a better energy efficiency),[6] the formation and reoxidation of the complex oxide deposit (denoted PbO_x) cannot be neglected in the model. As a first approximation, it is assumed that the complex oxide is formed from deposited PbO_2 during discharge and reoxidized to PbO_2 during the subsequent charge, consistent with the experimental observations. The precise mechanism, of course, involves other species, such as water, oxygen, and protons. A possible (electrochemical) mechanism, with $x = 1$, is

$$PbO_2 + 2e^- + 2H^+ \rightleftharpoons PbO + H_2O \qquad [3]$$

involving multiple steps. Other mechanisms may involve lead hydroxides. However, because the mechanism and participating species are not known precisely, a general form for the reaction rate is assumed below (Eq. 28), with a dependence on the positive-electrode overpotential, temperature, and complex-oxide concentration, while the dependence on the other unknown species is neglected.

Equations.— Let c_i, where i = Pb(II), H_2O, and H^+, denote the concentration of species i in the liquid electrolyte. A volume-averaged mass balance for each species can be expressed in the following form

$$\frac{\partial c_i}{\partial t} + \nabla \cdot \mathbf{N}_i = 0 \qquad [4]$$

For the concentration fluxes $\mathbf{N}_i$, modified Nernst–Planck equations are used,[27,29] which account for the transport of each charged species by hydrodynamic dispersion, electrokinetic effects, and convection. The total flux for the *i*th species is

$$\mathbf{N}_i = -D_i \nabla c_i - \frac{z_i c_i D_i}{RT} F \nabla \phi + \mathbf{u} c_i \qquad [5]$$

where $\mathbf{u} = (u,v)$ is the liquid electrolyte velocity, ϕ is the ionic potential, D_i and z_i are the diffusion coefficient and valence for species i, respectively, T is the temperature of the electrolyte solution, and R is the molar gas constant. The electrolyte is considered to be electrically neutral and to be governed by the condition

$$\sum_i z_i c_i = 0 \qquad [6]$$

which is used to calculate the concentration of HSO_4^-. The bulk flow velocity of the electrolyte solution, $\mathbf{u}$, is given by the incompressible Navier–Stokes equations (according to the assumptions above)

$$\rho \frac{\partial \mathbf{u}}{\partial t} + \rho(\mathbf{u}\cdot\nabla)\mathbf{u} = -\nabla p + \mu \nabla^2 \mathbf{u} \qquad [7]$$

$$\nabla \cdot \mathbf{u} = 0 \qquad [8]$$

where p is the pressure, ρ is the density, and μ is the averaged dynamic viscosity of the liquid solution. In keeping with the dilute-solution approximation and the incompressibility assumption, a constant value for μ was used.

Summing over the current densities arising from each species, $z_i\mathbf{N}_i$, the total current density in the electrolyte can be calculated, using the electroneutrality condition, as follows

$$\mathbf{j}_e = \sum_i z_i \mathbf{N}_i = -\kappa \nabla \phi - F \sum_i z_i D_i \nabla c_i \qquad [9]$$

where the ionic conductivity κ is given by

$$\kappa = \frac{F^2}{RT} \sum_i z_i^2 D_i c_i \qquad [10]$$

At all points, including the boundaries, the ionic and electronic currents satisfy the condition of charge conservation

$$\nabla \cdot \mathbf{j}_e + \nabla \cdot \mathbf{j}_s = 0 \qquad [11]$$

The total current $\mathbf{j} = \mathbf{j}_e + \mathbf{j}_s$ is divergence free; it is purely ionic in the solution phase and purely electronic in the metal conductors.

Rearranging Eq. 9 yields an expression for the potential gradient, which is needed to calculate the migration term in the flux, $\mathbf{N}_i$ for charged species i

$$\nabla \phi = -\frac{\mathbf{j}_e}{\kappa} - \frac{F}{\kappa} \sum_i z_i D_i \nabla c_i \qquad [12]$$

As a first approximation, the PbO_2 and PbO_x concentrations on the electrode surface are assumed to be uniform and vary with time according to the following mass balances

$$\frac{\partial c_{PbO_x}}{\partial t} = \frac{j_{PbO_x}}{F}$$

$$\frac{\partial c_{PbO_2}}{\partial t} = \frac{j_{PbO_2}}{F} - \frac{j_{PbO_x}}{F} \qquad [13]$$

where j_{PbO_x} is the current associated with PbO_x formation/oxidation. j_{PbO_2} and j_{Pb} are used to denote the x (normal) components of the current density that is consumed during the redox reactions at the PbO_2/Pb(II) and Pb/Pb(II) electrodes, respectively (see below). At the negative electrode, the Pb concentration satisfies

$$\frac{\partial c_{Pb}}{\partial t} = \frac{j_{Pb}}{F} \qquad [14]$$

Boundary conditions.— For the specification of the boundary conditions, the reader is referred to Fig. 2. At the electrode surfaces, separate electrochemical reactions take place, locally consuming the Pb(II) during charge and generating Pb(II) during discharge. Water is consumed and protons are generated at the PbO_2/Pb(II) electrode surface during charge (see Reactions 1 and 2), and the reverse is true during discharge. The source terms for these species enter through the boundary conditions, applied at the electrode surfaces. The following conditions hold at the Pb/Pb(II) electrode surface

$$-\mathbf{N}_{Pb(II)} \cdot \mathbf{n} = -\frac{j_{Pb}}{2F}$$

$$-\mathbf{N}_{H_2O} \cdot \mathbf{n} = 0$$

$$-\mathbf{N}_{H^+} \cdot \mathbf{n} = 0 \qquad [15]$$

while at the PbO_2/Pb(II) electrode surface

$$-\mathbf{N}_{Pb(II)} \cdot \mathbf{n} = -\frac{j_{PbO_2}}{2F}$$

$$-\mathbf{N}_{H_2O} \cdot \mathbf{n} = -\frac{j_{PbO_2}}{F}$$

$$-\mathbf{N}_{H^+}\cdot\mathbf{n} = 2\frac{j_{PbO_2}}{F} \quad [16]$$

where the terms j_{PbO_2} and j_{Pb} refer to the x (normal) components of the current density that is consumed during the redox reactions at the PbO_2/Pb(II) and Pb/Pb(II) electrodes, respectively (see below). The conditions above ensure that charge conservation is satisfied, according to Eq. 11

$$\text{Pb/Pb(II) electrode: } \mathbf{j}_e\cdot\mathbf{n} = -\frac{j_{Pb}}{F}$$

$$PbO_2\text{/Pb(II) electrode: } \mathbf{j}_e\cdot\mathbf{n} = \frac{j_{PbO_2}}{F} \quad [17]$$

Along the electrode surfaces, a Neumann condition was applied for the pressure

$$\nabla p\cdot\mathbf{n} = 0 \quad \text{(electrode surfaces)} \quad [18]$$

At the inlets, the liquid electrolyte solution enters with a prescribed bulk velocity and the species concentrations are given

$$c_i = c_i^{in}(t) \text{ and } \mathbf{u} = (0, v_{in}) \quad \text{(inlets)} \quad [19]$$

The dynamic inlet concentrations c_i^{in} are determined from a mass balance that takes into account the recirculation of the electrolyte (described below). At the electrode surfaces, no-slip conditions are applied

$$\mathbf{u} = 0 \quad \text{(electrode surfaces)} \quad [20]$$

At the outlets, the liquid pressure is prescribed and the diffusive fluxes of the species are set to a zero value (fully developed flow conditions)

$$-D_i^{eff}\nabla c_i\cdot\mathbf{n} = 0 \quad p = p_{out} \quad \text{(outlets)} \quad [21]$$

Consistent initial conditions are prescribed for the concentrations and potentials as follows: At the Pb/Pb(II) (negative) electrode

$$c_i = c_i^0$$

$$V_- = E_-$$

$$\phi = 0 \quad [22]$$

and at the PbO_2/Pb(II) (positive) electrode

$$c_i = c_i^0$$

$$V_+ = E_+$$

$$\phi = 0 \quad [23]$$

where V_+ and V_- are the electronic potentials along the PbO_2/Pb(II) and Pb/Pb(II) electrode surfaces, respectively, and E_+ and E_- are the open-circuit potentials for Reactions 1 and 2, respectively.

In a typical experimental arrangement, the cell voltage during charge or discharge is measured from the potential difference across an open-circuit cell, i.e., with conditions pertaining to the cell outlets. In the simulations, the cell voltage, E_{cell}, was measured with respect to the potentials at the intersections between the current collectors and electrodes, along $y = h$ in Fig. 2.

In the real system, the movement of the electrolyte solution through the battery, pump, and reservoir alters the concentrations at the inlet boundaries with time. It is essential to capture at least the main features of this process because the flow rate is the main variable used to control the distribution of the electrolyte, and variations in v_{in} can markedly affect the performance of the battery.

Invoking conservation of volume, the volumetric flow at the outlet boundary, which has a cross-sectional area A_{out}, is $Q = v_{in}A_{out}$. From the calculated average concentration at the outflow boundary

Table I. Default values of the constants related to electrochemistry.

Symbol	Quantity	Value
ν_1	Reaction order for PbO_x in Eq. 28	2
ν_2	Reaction order for PbO_2 in Eq. 28	1
ν_3	Reaction order for H^+ in Eq. 28	1
k_0^{Pb}	Rate constant for Reaction 1	2.1×10^{-7} m s^{-1} [a]
$k_0^{PbO_2}$	Rate constant for Reaction 2	2.5×10^{-7} m s^{-1} [a]
K_0^f	Forward rate constant in Eq. 28	2.0×10^{-10} m^4 mol^{-1} s^{-1} [a]
K_0^b	Backward rate constant in Eq. 28	4.5×10^{-7} m^4 mol^{-1} s^{-1} [a]
E_-^0	Formal potential: Pb(II)/Pb[4]	−0.3 V
E_+^0	Formal potential: Pb(II)/PbO_2[4]	1.63 V

[a] Fitted parameter.

$$c_i^{out} = \int_{y=h} c_i dx$$

the inlet concentrations are approximated from the following mass balance, which assumes instantaneous mixing and negligible reaction in the reservoir, which contains a volume V_r of the electrolyte

$$\frac{dc_i^{in}}{dt} = \frac{Q}{V_r}(c_i^{out} - c_i^{in})$$

$$c_i^{in}(0) = c_i^0 \quad [24]$$

As defined above, c_i^0 is the initial concentration of species i. The total volume of electrolyte V is the sum of the internal cell and the reservoir volumes, hdw and V_r respectively, where h is the height of the cell, w is the gap between the PbO_2/Pb(II) and Pb/Pb(II) electrode surfaces, and d is the depth of the electrodes (into the page in Fig. 2). It is assumed that the volume in the connecting tubes is negligible.

Reaction kinetics and cell voltage.— The simplest description of the reversible redox reactions taking place at the electrode surfaces is the Butler–Volmer expression for charge-transfer kinetics[18]

$$j_{Pb} = Fk_0^{Pb}c_{Pb(II)}\left[\exp\left(\frac{F\eta_-}{RT}\right) - \exp\left(-\frac{F\eta_-}{RT}\right)\right]$$

$$j_{PbO_2} = Fk_0^{PbO_2}c_{Pb(II)}\left(\frac{c_{H^+}}{c_{H^+}^0}\right)\left[\exp\left(\frac{F\eta_+}{RT}\right) - \exp\left(-\frac{F\eta_+}{RT}\right)\right] \quad [25]$$

for the Pb/Pb(II) and PbO_2/Pb(II) electrodes, respectively. In these expressions, k_0^{Pb} and $k_0^{PbO_2}$ are the rate constants for Reactions 1 and 2, respectively, and η_- and η_+ are the overpotentials at the Pb/Pb(II) and PbO_2/Pb(II) electrodes, respectively. The common approximation of equal charge-transfer coefficients for the forward and reverse reactions has been made for the reactions at both electrodes (values equal to 1 at both electrodes for a two-electron transfer). The overpotentials are defined by

$$\eta_\pm = V_\pm - \phi - E_\pm \quad [26]$$

where E_+ and E_- are the open-circuit potentials for Reactions 1 and 2, respectively. They are estimated values from the relevant Nernst equations using concentrations as approximations for the activities

$$E_- = E_-^0 + \frac{2.3RT}{F}\ln\ c_{Pb(II)}$$

$$E_+ = E_+^0 - \frac{2.3RT}{F}(\ln\ c_{Pb(II)} - \ln\ c_{H^+}) \quad [27]$$

The formal electrode potentials for the Pb/Pb(II) and PbO_2/Pb(II) electrodes, E_-^0 and E_+^0, respectively, are given in Table I. The ionic

potential was fixed at 0 V along the PbO_2/Pb(II) electrode surface because only potential differences are meaningful. It is assumed that the electric current is applied uniformly along the Pb/Pb(II) electrode surface, parallel to the x axis in Fig. 2.

To describe the kinetics of formation and reoxidation of the PbO_x deposit at the positive electrode, a general Butler–Volmer expression was used

$$\text{PbO}_2/\text{Pb(II)electrode:} j_{\text{PbO}_x} = F\left[K_0^{\text{f}}(c_{\text{PbO}_x})^{\nu_1}\exp\left(\frac{F\eta_+}{RT}\right) - K_0^{\text{b}}(c_{\text{PbO}_2})^{\nu_2}(c_{\text{H}^+})^{\nu_3}\exp\left(\frac{-F\eta_+}{RT}\right)\right] \quad [28]$$

where ν_1, ν_2, and ν_3 are the reaction orders in PbO_x, PbO_2, and H^+, respectively. This assumed form takes into account the possible dependence on the proton and two lead-oxide concentrations, as discussed in the Reaction Mechanisms section. Deviations from η_+ for the side-reaction overpotential have been absorbed into the reaction constants K_0^{f} and K_0^{b}. The charge balance at the positive electrode can now be expressed as

$$\text{PbO}_2/\text{Pb(II)} \ \text{electrode:} \ j_{\text{app}} = j_{\text{PbO}_x} + j_{\text{PbO}_2} \quad [29]$$

where j_{app} is the current density applied to the electrode surfaces. Resolving Eq. 12, with the assumption that the current density is applied in the direction normal to the Pb/Pb(II) electrode surface, gives

$$\frac{\partial \phi}{\partial y} = -\frac{F}{\kappa}\sum_{\text{i}} z_{\text{i}}D_{\text{i}}\frac{\partial c_{\text{i}}}{\partial y}$$

$$\frac{\partial \phi}{\partial x} = -\frac{j_{\text{app}}}{\kappa} - \frac{F}{\kappa}\sum_{\text{i}} z_{\text{i}}D_{\text{i}}\frac{\partial c_{\text{i}}}{\partial x} \quad [30]$$

Integrating the second of these equations in the x direction from the PbO_2/Pb(II) to the Pb/Pb(II) electrode ($x = 0$ to $x = w$) yields

$$\phi(w,y) = -\int_0^{\text{w}}\left(\frac{j_{\text{app}}}{\kappa} + \frac{F}{\kappa}\sum_{\text{i}} z_{\text{i}}D_{\text{i}}\frac{\partial c_{\text{i}}(\psi,y)}{\partial \psi}\right)d\psi \quad [31]$$

along the Pb/Pb(II) electrode surface $x = w$. The prescribed value of $\phi = 0$ along $x = 0$ has been used in the derivation above. Having determined the ionic potential at the Pb/Pb(II) electrode surface and with the prescribed value at the PbO_2/Pb(II) electrode surface, it is possible to calculate the electronic potential along the PbO_2/Pb(II) and Pb/Pb(II) electrode surfaces, $V_+(y)$ and $V_-(y)$, respectively, using the Butler–Volmer expression 25 and the definitions of the overpotentials 26

$$V_-(y) = \eta_-(y) + E_- + \phi_-(w,y)$$

$$V_+(y) = \eta_+(y) + E_+ \quad [32]$$

where

$$\eta_-(y) = \frac{RT}{F}\sinh^{-1}\left(-\frac{j_{\text{app}}/F}{k_0^{\text{Pb}}c_{\text{Pb(II)}}}\right) \quad [33]$$

and η_+ is determined numerically from the implicit Eq. 29 using Eq. 25 and 28. The cell voltage is calculated as the difference between the electronic potential values at the two electrodes, evaluated at the outlets in both cases

$$E_{\text{cell}} = V_+ - V_- \quad [34]$$

Numerical Details

The initial-boundary value problem outlined above was solved using the finite-volume methodology, with a first-order spatial discretisation[30] and a first-order Euler scheme for the time stepping.

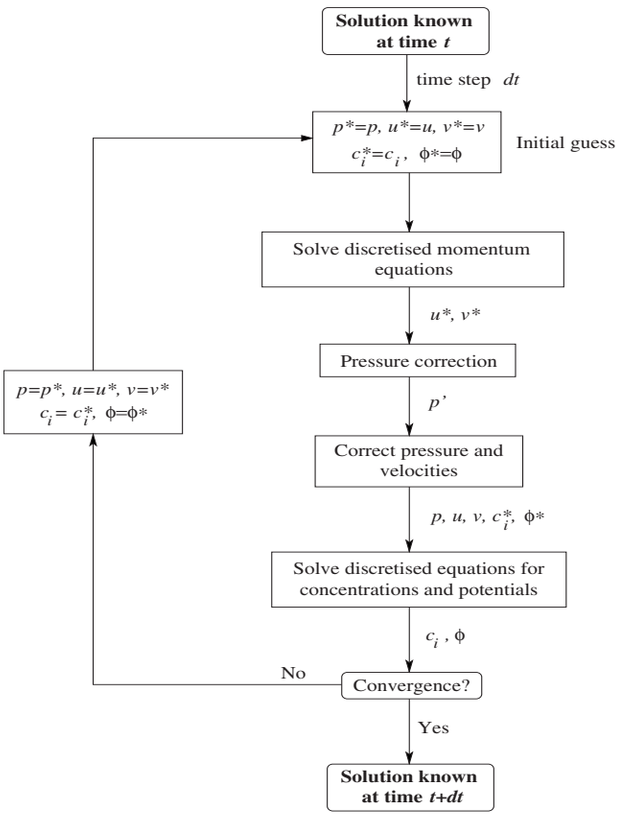

Figure 3. A schematic of the algorithm flow.

To eliminate pressure oscillations and to ensure stability, the problem was formulated on a staggered grid, and an upwind differencing scheme was employed. The Navier–Stokes equations for the liquid electrolyte flow velocity and pressure were solved using the SIMPLE algorithm.[31] The flow of the algorithm is depicted in Fig. 3, in which starred quantities represent intermediate values in the iterative step of the SIMPLE algorithm. The pressure field is guessed, p^*, based on the current value, $p(t)$, and is used to calculate the intermediate velocities u^* and v^*. A Poisson equation for the pressure correction p', with a source term dependent on u^* and v^*, is subsequently solved to correct the pressure and velocity values.[31]

In the practical implementation of the algorithm, the pressure and velocity corrections were under-relaxed[30] by a factor of $\alpha = 0.3$ to improve stability, a standard procedure. The discretized equations for the concentrations and potential gradient were then solved explicitly, in time, using an iterative tridiagonal matrix algorithm (TDMA).[30] The ordinary differential Eq. 24 and 13 were solved using the Euler method. An iteration loop was applied to the entire process (between each time step) to ensure convergence toward a solution at the advanced time: $\|\Delta v/v_{\text{in}}\|_\infty < 1 \times 10^{-5}$, where Δv is the difference between the intermediate updated solution at time $t + dt$ and the known solution at time t for the y flow velocity, and $\|\psi\|_\infty = \max_{\text{i,j}} \ \psi(i\Delta y, j\Delta x)$ denotes the discrete sup norm. The equations for the intermediate velocity components were solved explicitly, while the Poisson equation for the pressure correction was solved implicitly using the iterative TDMA. The Navier–Stokes solver was tested on the lid-driven cavity problem[32] to ensure stability and accuracy. The numerical scheme was implemented in Matlab.

The explicit time marching and the direct solution of the linear system for the pressure correction did not impose severe restrictions on the solution time, although the code could readily be optimized with an implicit scheme together with a sparse solver. Due to the

Table II. Default values for constants related to the transport of charge and mass.

Symbol	Quantity	Value
$D_{Pb(II)}$	Pb(II) diffusion coefficient in electrolyte[33]	2.4×10^{-10} m^2 s^{-1}
D_{H_2O}	Water diffusion coefficient in electrolyte[34]	2.3×10^{-9} m^2 s^{-1}
D_{H^+}	Proton diffusion coefficient in the electrolyte[35]	1.4×10^{-9} m^2 s^{-1}
$D_{HSO_4^-}$	HSO_4^- diffusion coefficient in the electrolyte[36]	1.23×10^{-9} m^2 s^{-1}
μ_{H_2O}	Water viscosity	10^{-3} Pa s

first-order nature of the spatial discretization, a minimum resolution of 20 × 20 uniformly sized cells was required to achieve acceptable convergence between successively finer grids, along with a maximum time step of 0.1 s. The lowest resolution used for the calculations below was 25 × 25 uniformly sized cells, and the maximum time step was 0.1 s, for which the base case below (two full charge–discharge simulation over 12,538 s with Matlab visualization steps included) took 10,634 s central processing unit time on a dual-core Athlon 4600 + 64-bit machine with 4 Gbytes of random access memory. At this level of resolution, typically three to five iterations were required in the outer loop to meet the inner loop criterion.

Parameter fitting.— As is invariably the case for models of complex systems, adjustment of certain parameters was required to achieve a match between the simulation results and the experimental data. Due to the level of detail included, however, the number of such parameters was kept low. The rate constants k_0^{Pb} and $k_0^{PbO_2}$ were fitted to experimental data for first charge and discharge cycles (when the side reaction rate is negligible). The value of the reaction constant for the side reaction, $k_0^{PbO_x}$, and the reaction order, ν, were adjusted to capture the correct qualitative behavior during the second charge phase when the oxidation of the complex oxide deposit takes place. A value of $\nu = 2$ yielded a closer match than the linear reaction order $\nu = 1$, which led to a sharp transition in the cell voltage as Reaction 2 began to dominate.

The cell voltage can be decomposed into several components, representing the various resistances in the cell

$$E_{cell} = E_- - E_+ - \sum_j |\eta_j| - i_{app} \sum_k R_k \qquad [35]$$

where the η_j are overpotentials due to charge-transfer resistances, mass transfer resistances, leaks and contact resistances, and the R_k are charge transport (ohmic) resistances. To match the experimentally measured open-circuit potential, a constant potential difference was added to the simulation results; i.e., they were shifted vertically downward by a constant value of 0.125 V in all cases. This requirement was likely to be due to resistances that were not included in the model, such as contact resistances, though the major components in Eq. 35 were explicitly included in the model.

The final fitting parameter was the initial proton concentration. Stable experimental curves were extracted from tests involving large numbers of charge/discharge cycles. The cycle number extracted was different for each case, and the run times at the points of extraction differed by up to 76 h. Because the proton concentration can change markedly over time,[4-9] the extracted curves corresponded to different (unknown) initial values for the simulation. For the purposes of simulation below, an initial value of 50 mol m^{-3} was selected to fit the simulated charge–discharge curve at $j_{app} = 20$ mA cm^{-2} to the experimental data. The same value was subsequently employed at the other current density values. A nonzero initial proton concentration leads to a nonzero initial state of charge.

The default set of parameter values for the simulations is given in Tables I-IV. These values were used unless otherwise stated.

Results and Discussion

In this section, simulation results are described and the numerical code is validated against experimental data. Experiments were performed at three current densities using 10 × 10 cm active surface area electrodes, with a mean linear flow velocity of $v_{in} = 2.3$ cm s^{-1}, as described in the Experimental section. The coulombic efficiency is defined as

$$\xi_c = \frac{j_{app}^d t_d}{j_{app}^c t_c} \qquad [36]$$

where j_{app}^c is the charge current density, j_{app}^d is the discharge current density, t_c is the time to charge, and t_d is the time to discharge. The charge capacity (usually expressed in Ah) during charge is defined as

$$C_c = \int_0^{t_c} I dt \qquad [37]$$

for a load I (A). A similar definition applies during discharge.

Validation and character of the solutions.— Figure 4 compares the experimentally obtained curves with the simulated cell voltage curves for a flow rate of $v_{in} = 2.3$ cm s^{-1} for different current density values. In each simulation, the cell was charged for 1 h, maintained at zero current density for 20 s, discharged for 1 h, maintained at zero current density for 20 s, charged for 1 h, maintained at zero current density for 20 s, and, finally, discharged until the cell voltage reached a value of 1.1 V. The curves shown in Fig. 4 represent the second charge/discharge cycles. There is good qualitative agreement between the two sets of curves in the trends observed during the charge and discharge phases as the current density is varied. There are, however, discrepancies in the time to discharge at 10 mA cm^{-2} and in the shape of the charge curve at 30 mA cm^{-2}, but the essential behavior is correctly captured. As the applied current density is increased, the cell voltage increases during charge, and the drop in cell voltage between charge and discharge increases. This is primarily due to the increased ohmic resistances as the cur-

Table III. Default initial and boundary values.

Symbol	Quantity	Value
T	Operating temperature	27 C
$c_{Pb(II)}^0$	Initial Pb(II) concentration	500 mol m^{-3}
$c_{H_2O}^0$	Initial water concentration	4.7×10^4 mol m^{-3}
$c_{HSO_4^-}^0$	Initial HSO_4^- concentration	1050 mol m^{-3}
$c_{H^+}^0$	Initial H^+ concentration	50 mol m^{-3}
p_{out}	Pb/Pb(II) electrode outlet pressure	300 kPa
v_{in}	Mean linear inlet flow velocity	0.023 m s^{-1}
j_{app}	Applied current density (charge)	200 A m^{-2}

Table IV. Default values of the constants related to structure.

Symbol	Quantity	Value
A	Active electrode surface area	0.01 m^2
A_{out}	Inlet/outlet cross section area	1.2×10^{-3} m^2
d	Electrode depth	0.1 m
h	Electrode height	0.1 m
V_r	Reservoir volume	1.38×10^{-3} m^3
w	Interelectrode separation	0.012 m

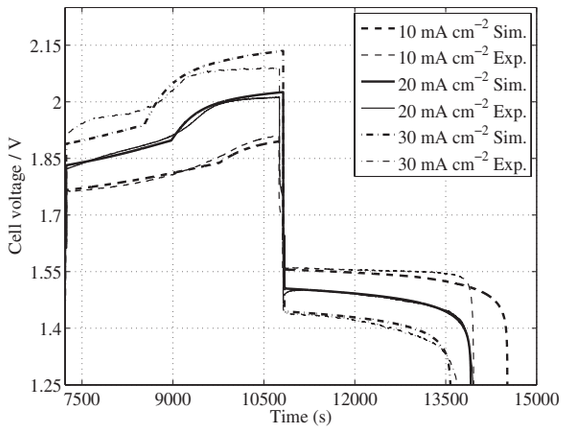

Figure 4. A comparison of experimental and simulated charge–discharge cell voltage curves for three applied current densities, j_{app}. In each simulation, the charge–discharge curve represents the second cycle: charge for 1 h, discharge for 1 h, followed by charge for 1 h, and discharge for 1 h (see Fig. 5).

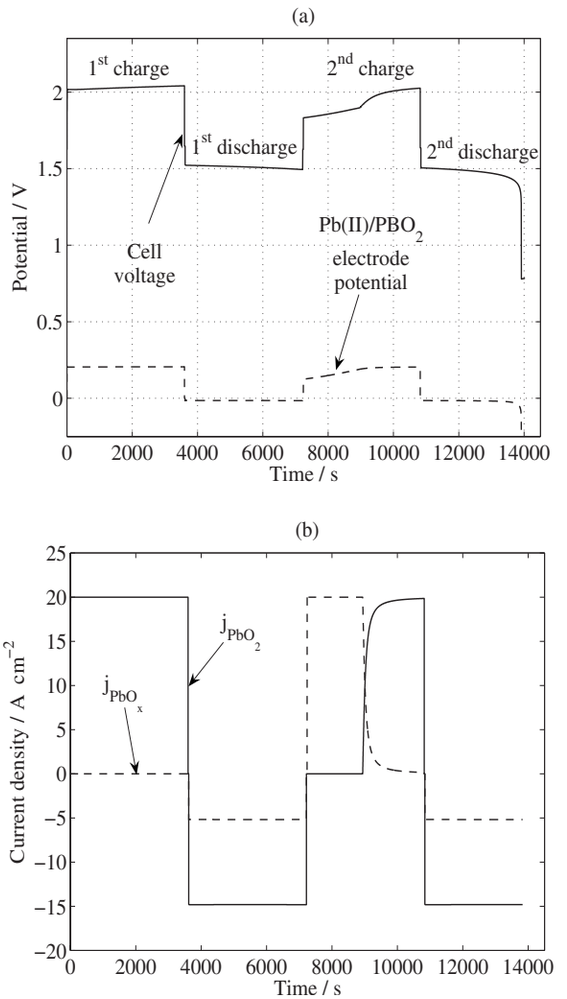

Figure 5. (a) The full simulated charge–discharge cell voltage and positive-electrode overpotential curves in $j_{app} = 20$ mA cm^{-2} in Fig. 4. (b) The current densities j_{PbO_2} and j_{PbO_x} associated with Reaction 2 and the side reaction, respectively, for an applied current density $j_{app} = 20$ mA cm^{-2}.

rent density is increased, as indicated in Eq. 35; an examination of Eq. 33 reveals that an increased value of j_{app} leads directly to an increase in the overpotentials at fixed concentrations, i.e., a greater potential difference is required to maintain a higher current density at fixed concentration values.

Both the experimental and simulation results show that the coulombic efficiency decreases as current density is increased; i.e., the time to reach a full (second) discharge decreases. The discrepancies in the times are likely to be a consequence of the uncertainty in the proton concentrations, which, as mentioned above, vary with time; the experimental curve corresponding to $j_{app} = 10$ mA cm^{-2} was taken after approximately 98 h, the curve corresponding to $j_{app} = 20$ mA cm^{-2} at around 28 h, and the curve corresponding to $j_{app} = 30$ mA cm^{-2} at around 9 h. Specifically, the state of charge for each experiment is not known precisely; thus, the simulations are only approximations to the actual cycles. The increased coulombic efficiency is discussed in the next section where the two cases $j_{app} = 10$ mA cm^{-2} and $j_{app} = 20$ mA cm^{-2} are compared.

Figure 5a shows the full charge/discharge simulation (over both cycles) for the case $j_{app} = 20$ mA cm^{-2} in Fig. 4, along with the corresponding overpotential at the positive Pb(II)/PbO_2 electrode. This figure clearly demonstrates the difference in character between the first and second charge phases, the second-charge curve taking on the shape described in the previous section:[4-9] PbO_x (the complex oxide) is oxidized from the surface of the positive electrode at the beginning of the second charge, which lowers the cell voltage substantially from the theoretical value. Figure 5a also shows that the shape of the cell voltage curve mirrors is indeed controlled by the overpotential at the positive electrode. The current densities j_{PbO_2} and j_{PbO_x} associated with Reaction 2 and the side reaction, respectively, are shown in Fig. 5b for the same applied current density of 20 mA cm^{-2}. The anode overpotential is heavily influenced by the side reaction. In the initial portion of the second charge phase, the side reaction consumes all of the applied current (up to $t \approx 9000$ s). As the PbO_x is depleted, j_{PbO_2} decays rapidly and at around $t = 9000$ s.

Contour plots of the Pb(II) reactant concentration during charge and discharge in $j_{app} = 20$ mA cm^{-2} are shown in Fig. 6a and b, with the positive electrode placed at $x = 0$ and the negative electrode at $x = 12$ mm. The contours correspond to (a) midway through the second charge ($t = 9040$ s) and (b) midway through the second discharge ($t = 12{,}245$ s). During charge, the minima in the Pb(II) and water (not shown) concentrations and the maximum in the proton concentration (not shown) are attained at the electrode surfaces in the vicinity of the outlet at $y = 10$ cm. Conversely, the maxima in the Pb(II) and water concentrations and the minimum in the proton concentration are attained at the same location during discharge. This pattern results from the locations of the reactions (along the electrode surfaces) and the recirculation of the electrolyte, during which reactants are replenished at the inlet from the reservoir solution. In the reservoir, the concentrations vary on a longer time scale due to mixing with a large volume of electrolyte with a composition close to its initial state. The time to full discharge is controlled by the proton concentration, which decays to zero at the interface between the outlet and the positive electrode (where protons are consumed according to the backward Reaction 2). This is confirmed in the next section.

The flow field exerts an influence on the distribution of reactants, as demonstrated in Fig. 7, which shows (a) the flow velocity vectors and (b) the y component of velocity during the charge–discharge simulation at $j_{app} = 20$ mA cm^{-2}. The x component of the flow velocity is practically negligible and is, therefore, not shown. The flow is established early in the simulation and remains steady thereafter. As a consequence of the no slip condition, the y component of the velocity decreases to zero as the electrode surfaces are approached. At a distance of 1.5 mm in the x direction from both electrode surfaces, the y component of the velocity is approximately

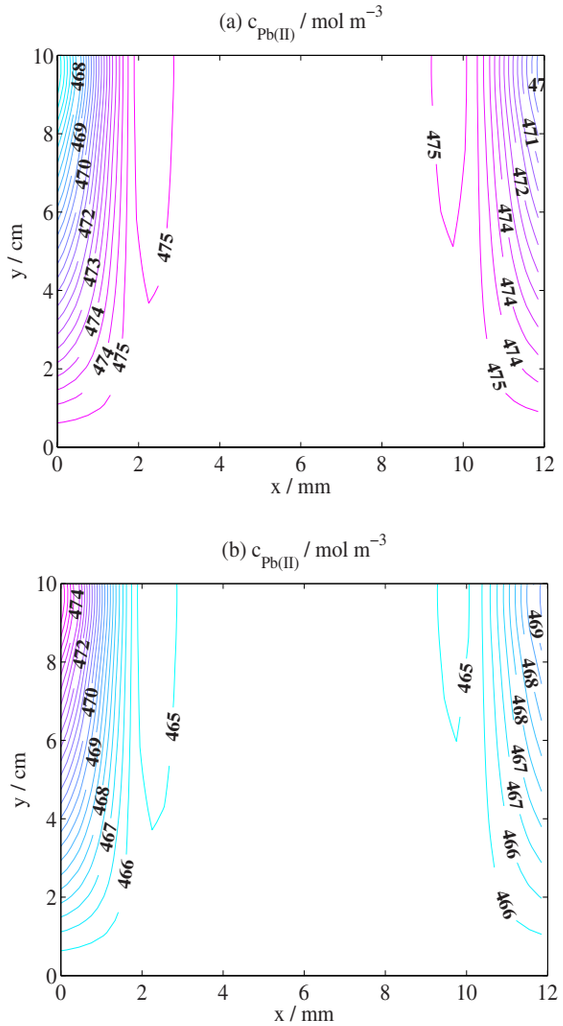

Figure 6. (Color online) Simulated Pb(II) concentration profiles (in mol m^{-3}) for v_{in} = 2.3 cm s^{-1} and j_{app} = 20 mA cm^{-2} in Fig. 4: (a) 9040 s (midway through the second charge) and (b) 12245 s (midway through the second discharge).

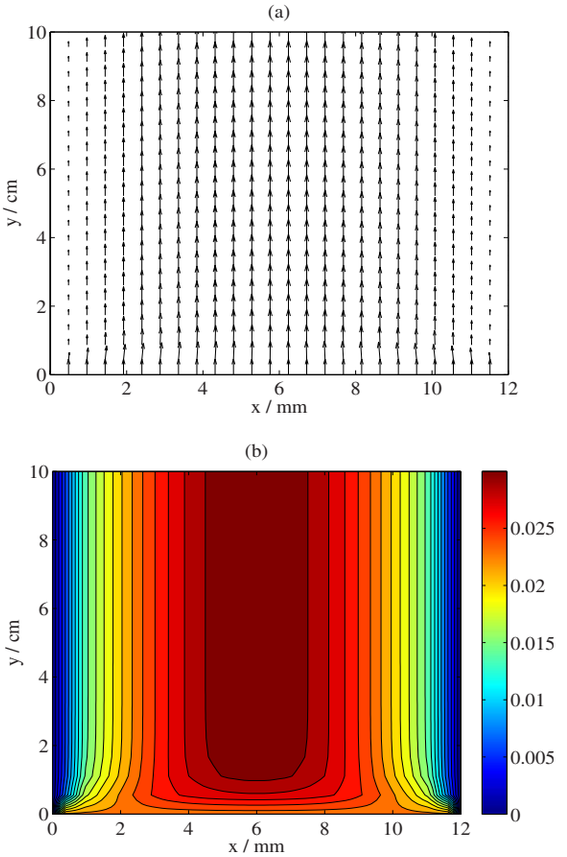

Figure 7. (Color online) Evolution of (a) the flow velocity vectors and (b) the y component of velocity (in cm s^{-1}) during the charge–discharge simulation with v_{in} = 2.3 cm s^{-1} and j_{app} = 20 mA cm^{-2} in Fig. 4 (corresponds to end of the first charge, with negligible variation at other times).

half its maximum value, which is attained at the center of the cell away from the inlet. The flow develops a parabolic profile away from the inlet, which can be seen from both Fig. 7a and b. There is a tendency for flow toward the center of the cell at the inlet, as a consequence of the zero velocity at the electrode surfaces. In the regions close to the electrode surfaces, convective transport of the reactants is less effective and, conversely, migration and diffusion play a more important role.

The effects of current density.— The effect of current density on the extent of the Pb(II) reactant depletion is demonstrated in Fig. 8, which shows simulated Pb(II) concentration profiles at the end of the second charge (t = 10,800 s) for j_{app} = 10 and 20 mA cm^{-2} and v_{in} = 2.3 cm s^{-1} in both cases. Comparing Fig. 8a and b reveals that the Pb(II) concentration is more uniform at the lower current density, a direct consequence of the slower rates of reaction at the electrodes. The difference between the lowest and highest concentrations of Pb(II) is approximately 5 mol m^{-3} for j_{app} = 10 mA cm^{-2}, whereas the difference for j_{app} = 20 mA cm^{-2} is approximately 13 mol m^{-3}. Similar differences are found in the water and proton concentrations.

The current densities j_{PbO_2} and j_{PbO_x} associated with Reaction 2 and the side reaction, respectively, are shown in Fig. 9a for the case j_{app} = 10 mA cm^{-2} in Fig. 4. This figure is to be compared with Fig. 5b, which pertains to an applied current density j_{app} = 20 mA cm^{-2}. The two figures reveal a similar behavior, the main difference being the longer time taken at the lower current density for Reaction 2 to dominate, i.e., to consume all of the applied current. The smaller current density requires a longer time to oxidize the complex oxide from the electrode surfaces. For j_{app} = 10 mA cm^{-2}, the charge capacities consumed by the side reaction are 0.728 Ah during the second charge and 0.213 Ah during the second discharge, with 0.272 and 0.787 Ah consumed by Reaction 2, respectively. The equivalent values for j_{app} = 20 mA cm^{-2} are 1.03 and 0.41 Ah, with 0.97 and 1.59 Ah consumed by Reaction 2, respectively. These numbers illustrate that the fraction of the current consumed by the side reaction during the second charge increases with the increase in applied current density.

Apparently, the increased coulombic efficiency for j_{app} = 10 mA cm^{-2} is not caused by differences in the extent to which the side reaction consumes the applied current; the efficiency increases despite an increase in the fraction of current consumed. Figure 9b shows the evolution of the proton concentration at the intersection between the outlet and the positive electrode, y = 10 cm and x = 0 mm for the two cases j_{app} = 10 mA cm^{-2} and j_{app} = 20 mA cm^{-2}. Both curves demonstrate the substantial decrease in the rate of proton generation between the first and second discharges, as a consequence of the side reaction. The final times in the two curves, at which the concentrations reach zero values, coincide with the respective times at which the second discharge is complete

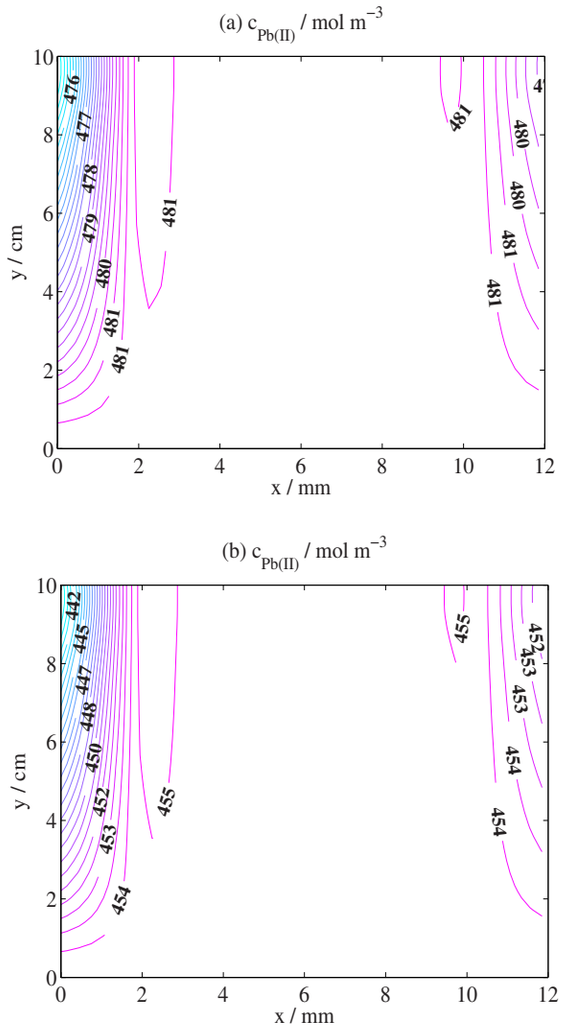

Figure 8. (Color online) The simulated Pb(II) concentration profiles (in mol m^{-3}) at end of the second charge $t = 10800$ s for (a) $j_{app} = 10$ mA cm^{-2} and (b) $j_{app} = 20$ mA cm^{-2}. The corresponding charge–discharge curves are shown in Fig. 4.

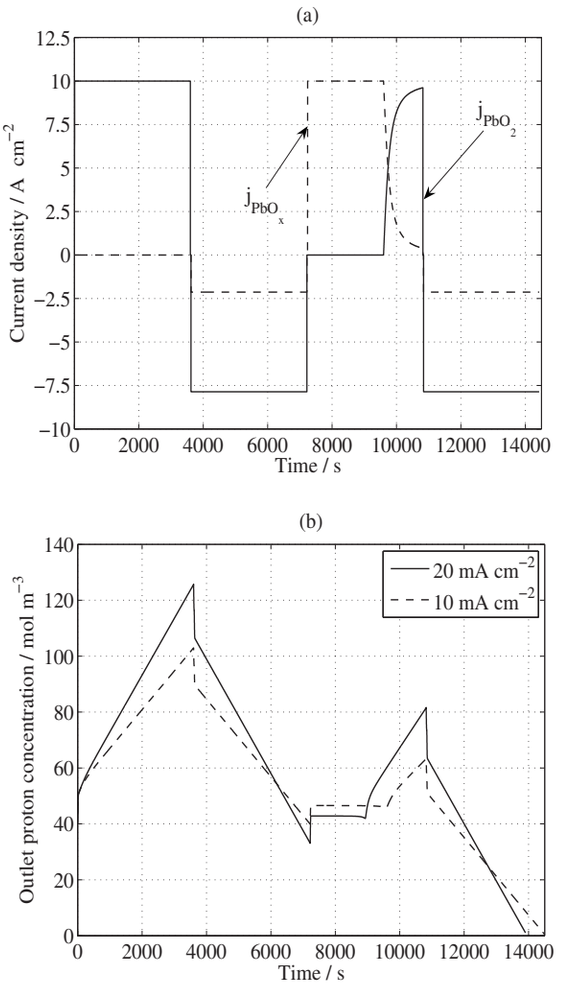

Figure 9. (a) The current densities j_{PbO_2} and j_{PbO_x} associated with Reaction 2 and the side reaction, respectively, for $j_{app} = 10$ mA cm^{-2} in Fig. 4. Compare with Fig. 5. (b) The evolution of the proton concentration at the intersection between the outlet and the positive electrode, $y = 10$ cm and $x = 0$ mm (see Fig. 2), for $j_{app} = 10$ mA cm^{-2} and $j_{app} = 20$ mA cm^{-2}.

(see Fig. 4); the times to discharge are determined by the proton concentration at $y = 10$ cm and $x = 0$ mm, where the positive overpotential is measured. The decreased coulombic efficiency at a higher current density is mainly a result of the increased concentration polarization and the concomitant increase in the anode overpotential to maintain the applied current. This is further indicated in Fig. 10, which shows the proton concentration profiles at the end of the first discharge ($t = 7200$ s) for (a) $j_{app} = 20$ mA cm^{-2} and (b) $j_{app} = 10$ mA cm^{-2}. At the lower current density, there is, approximately, a 22% difference between the maximum and minimum concentrations, and at the higher value the difference is approximately 37%. These differences are exacerbated during the second discharge.

Over longer charge times, the greater concentration polarization as the current density is increased would lead to faster rates of gas evolution through the greater overpotentials required to maintain the applied current density. At the moderate current densities covered in this paper, the overpotentials are low, and negligible gas evolution takes place. Extremes of operation, for example, nearing 100% state of charge or at current densities above 100 mA cm^{-2}, are incorporated into a more advanced model in subsequent papers.

Conclusions and Future Development

A transient model for the soluble lead-acid battery has been developed, taking into account the primary modes of reactant and charge transport, momentum conservation (Navier–Stokes equations), charge conservation, and a detailed model of the electrochemical reactions, including the critical formation and subsequent oxidation of a complex oxide layer on the positive electrode surface. A good qualitative match between the simulation results and experimental data was demonstrated, indicating that the underlying model is a sound basis for further development. Discrepancies can be attributed to the differences in the conditions between the simulations and experiments (such as proton concentration) and to components such as the current collectors, which were not included in this first model. Factors such as gas (oxygen and hydrogen) evolution and contact resistances could also play a role, and these are to be investigated in future work.

The simulation results strongly suggest that the two-step charge behavior of the dynamic lead-acid cell is controlled by the oxidation of the complex oxide layer on the positive electrode surface. The evolution of the overpotential at the positive electrode closely mirrors that of the cell voltage. This result has been confirmed experimentally[37] (Fig. 6 of that paper). The efficiency of the battery was predicted to decrease with an increase in the applied current

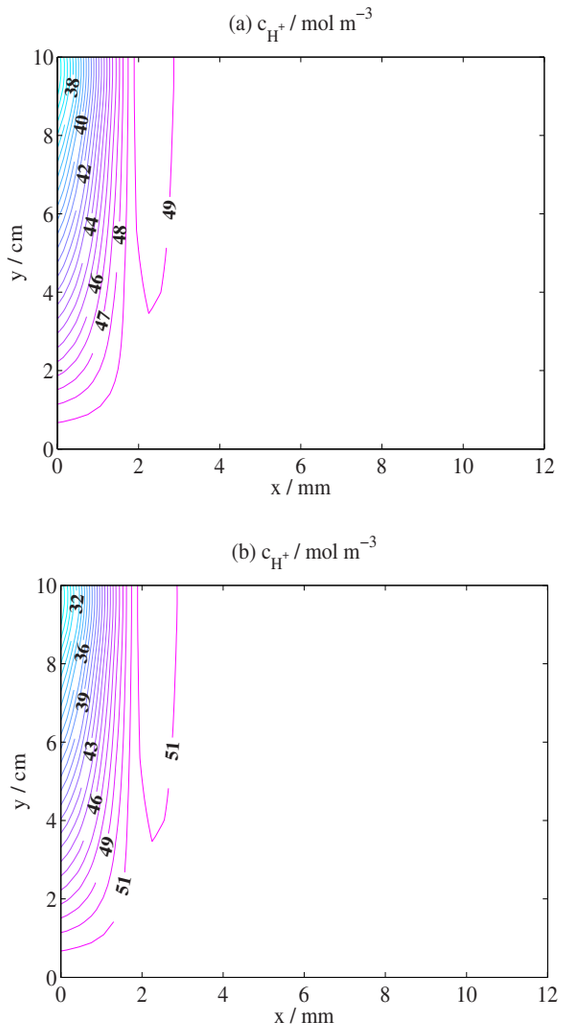

Figure 10. (Color online) Simulated proton concentration profiles (in mol m^{-3}) at the end of the first discharge (t = 7200 s) with v_{in} = 2.3 cm s^{-1} and (a) j_{app} = 10 mA cm^{-2} and (b) j_{app} = 20 mA cm^{-2}. The corresponding charge–discharge curves are shown in Fig. 4.

density, which again agrees with experiments under the operating conditions considered.[5] The decrease in the coulombic efficiency appears to be a result of increased proton concentration polarization during discharge, which leads to a simultaneously greater increase in the anode overpotential to maintain the current density.

In the present paper, the effects of the applied current density value on performance were investigated. In a forthcoming paper, a detailed parametric study is performed with respect to temperature, mean linear electrolyte flow rate, charge times, electrode dimensions, interelectrode gap, and reactant concentrations, with further comparisons to experimental data. Efforts to incorporate gas evolution and deposition of Pb and PbO_2 on the electrode surfaces, as well as to develop a better understanding of the complex anode kinetics, are also under way.

Acknowledgments

The authors are grateful for financial support from the Technology Strategy Board, U.K. They also acknowledge the support of partners, C-Tech Innovation Ltd. and E-ON UK Ltd.

Southampton University assisted in meeting the publication costs of this article.

List of Symbols

A	active surface area of electrodes, m^2
c	concentration, mol m^{-3}
C_c	charge capacity, Ah
d	electrode depth, m
D	diffusion coefficient, m^2 s^{-1}
e	numerical error (in concentrations), mol m^{-3}
E_{cell}	cell voltage, V
E^0	open-circuit voltage, V
F	Faraday's constant, C mol^{-1}
h	electrode height, m
k	rate constant, m s^{-1}
$\mathbf{j}$	current density, A m^{-2}
j_{app}	applied current density, A m^{-2}
K	rate constant, m^4 mol^{-1} s^{-1}
$\mathbf{n}$	unit outer normal dimensionless
$\mathbf{N}$	molar flux, mol m^{-3} s^{-1}
N	number of grid points dimensionless
p	pressure, Pa
Q	volumetric flow rate, m^3 s^{-1}
R	molar gas constant, J K^{-1} mol^{-1}
t	time, s
T	temperature, K
u	x velocity, m s^{-1}
V_r	reservoir volume, m^3
V	electronic potential, V
v	y velocity, m s^{-1}
x	horizontal distance, m
y	vertical distance, m
z	valence dimensionless

Greek

η	overpotential, V
κ	ionic conductivity, S m^{-1}
μ	dynamic viscosity, kg m^{-1} s^{-1}
ξ	efficiency dimensionless
ρ	density, kg m^{-3}
ϕ	ionic potential, V

Subscript

e	electrolyte property
E	energy
i	species i = Pb(II), PbO_x, H_2O, and H^+
in	inlet value
out	outlet value
s	solid property
*	intermediate value
′	correction

Superscript

in	inlet value
out	outlet value
0	initial value

References

1. C. Ponce de Léon, A. Frías-Ferrer, J. González-Garcia, D. A. Szánto, and F. C. Walsh, *J. Power Sources*, **160**, 716 (2006).
2. M. Skyllas-Kazacos and C. Menictas, in 19th International Telecommunications Energy Conference, 9–23 October, 1997, Melbourne Convention Centre, Melbourne, Australia.
3. D. P. Scamman, G. W. Reade, and E. P. L. Roberts, *J. Power Sources*, **189**, 1220 (2009).
4. A. Hazza, D. Pletcher, and R. Wills, *Phys. Chem. Chem. Phys.*, **6**, 1773 (2004).
5. D. Pletcher and R. Wills, *Phys. Chem. Chem. Phys.*, **6**, 1779 (2004).
6. D. Pletcher and R. Wills, *J. Power Sources*, **149**, 96 (2005).
7. A. Hazza, D. Pletcher, and R. Wills, *J. Power Sources*, **149**, 103 (2005).
8. D. Pletcher, H. Zhou, C. T. J. Low, G. Kear, and F. C. Walsh, *J. Power Sources*, **180**, 621 (2008).
9. D. Pletcher, H. Zhou, C. T. J. Low, G. Kear, and F. C. Walsh, *J. Power Sources*, **180**, 630 (2008).
10. H. Bode, *Lead-Acid Batteries*, John Wiley & Sons, New York (1977).
11. J. Newman and W. Tiedemann, *J. Electrochem. Soc.*, **144**, 3081 (1997).
12. C. Y. Wang, W. B. Gu, and B. Y. Liaw, *J. Electrochem. Soc.*, **145**, 3407 (1998).
13. C. Y. Wang, W. B. Gu, and B. Y. Liaw, *J. Electrochem. Soc.*, **145**, 3418 (1998).
14. M. Doyle, T. F. Fuller, and J. Newman, *J. Electrochem. Soc.*, **140**, 1526 (1993).
15. T. F. Fuller, M. Doyle, and J. Newman, *J. Electrochem. Soc.*, **141**, 1 (1994).
16. T. I. Evans, T. V. Nguyen, and R.E. White, *J. Electrochem. Soc.*, **136**, 328 (1989).
17. W. B. Gu, C. Y. Wang, S. M. Li, M. M. Geng, and B. Y. Liaw, *Electrochim. Acta*, **44**, 4525 (1999).

18. V. Srinivasan, G. Q. Wang, and C. Y. Wang, *J. Electrochem. Soc.*, **150**, A316 (2003).
19. P. Ramadass, B. Haran, R. White, and B. N. Popov, *J. Power Sources*, **123**, 230 (2003).
20. G. Ning and B. N. Popov, *J. Electrochem. Soc.*, **151**, A1584 (2004).
21. A. A. Shah, P. C. Sui, G. S. Kim, and S. Ye, *J. Power Sources*, **166**, 1 (2007).
22. A. A. Shah and F. C. Walsh, *J. Power Sources*, **185**, 287 (2008).
23. A. A. Shah, T. R. Ralph, and F. C. Walsh, *J. Electrochem. Soc.*, **156**, B465 (2009).
24. A. A. Shah, M. J. Watt-Smith, and F. C. Walsh, *Electrochim. Acta*, **53**, 8087 (2008).
25. M. Li and T. Hikihara, *IEICE Trans. Fundamentals*, **E91-A**, 1741 (2008).
26. X. Li, D. Pletcher, and F. C. Walsh, *Electrochim. Acta*, **54**, 4688 (2009).
27. J. Newman, *Electrochemical Systems*, Prentice-Hall, Englewood Cliffs, NJ (1991).
28. J. A. Sethian, *Level Set Methods*, Cambridge University Press, New York (1996).
29. R. F. Probstein, *Physicochemical Hydrodynamics*, Butterworth-Heinemann, Woburn, MA (1989).
30. H. K. Versteeg and W. Malalasekera, *An Introduction to Computational Fluid Dynamics: The Finite Volume Method*, Prentice-Hall/Pearson, Harlow, U.K. (1995).
31. S. V. Patankar, *Numerical Heat Transfer and Fluid Flow*, Hemisphere, New York (1980).
32. J. D. Bozeman and C. Dalton, *J. Comput. Phys.*, **12**, 348 (1973).
33. T. Yamamura, M. Watanabe, T. Yano, and Y. Shiokawa, *J. Electrochem. Soc.*, **152**, A830 (2005).
34. R. Mills, *J. Phys. Chem.*, **77**, 685 (1973).
35. M. W. Verbrugge and R. F. Hill, *J. Electrochem. Soc.*, **137**, 886 (1990).
36. G. E. Zaikov, A. P. Iordanskii, and V. S. Markin, *Diffusion of Electrolytes in Polymers*, VSP, Utrecht, The Netherlands (1988).
37. J. Collins, G. Kear, X. Li, C. T. J. Low, D. Pletcher, R. Tangirala, D. Stratton-Campbella, F. C. Walsh, and C. Zhang, *J. Power Sources*, **195**, 1731 (2010).